Check for updates

Geophysical Research Letters

RESEARCH LETTER
10.1029/2025GL121211

Ocean Meanders Modulate Extratropical Cyclone Energetics

Félix Vivant[1] and **Guillaume Lapeyre**[1]

[1]LMD-IPSL, ENS, PSL Université, Ecole Polytechnique, IP Paris, Sorbonne Université, CNRS, Paris, France

Key Points:

- Extratropical cyclone intensification is influenced by ocean meanders with strong temperature contrast and is modulated by their size
- Moisture supply above the warm side of a meander triggers diabatic heating within the cyclone a few hours later
- This enhances the eddy kinetic energy of the surface cyclone and of upper-level anomalies

Supporting Information:

Supporting Information may be found in the online version of this article.

Correspondence to:

F. Vivant,
felix.vivant@lmd.ipsl.fr

Citation:

Vivant, F., & Lapeyre, G. (2026). Ocean meanders modulate extratropical cyclone energetics. *Geophysical Research Letters*, *53*, e2025GL121211. https://doi.org/10.1029/2025GL121211

Received 10 DEC 2025
Accepted 4 APR 2026

Author Contributions:

Conceptualization: Félix Vivant, Guillaume Lapeyre
Data curation: Félix Vivant
Formal analysis: Félix Vivant
Funding acquisition: Guillaume Lapeyre
Investigation: Félix Vivant, Guillaume Lapeyre
Methodology: Félix Vivant, Guillaume Lapeyre
Software: Félix Vivant, Guillaume Lapeyre
Validation: Félix Vivant, Guillaume Lapeyre
Visualization: Félix Vivant
Writing – original draft: Félix Vivant, Guillaume Lapeyre
Writing – review & editing: Félix Vivant, Guillaume Lapeyre

© 2026. The Author(s).
This is an open access article under the terms of the Creative Commons Attribution License, which permits use, distribution and reproduction in any medium, provided the original work is properly cited.

Abstract Extratropical cyclones primarily develop over the western parts of ocean basins, where strong sea surface temperature (SST) contrasts form along western boundary currents. While previous studies have highlighted the influence of the mean SST and SST gradient on cyclones developing over these currents, they have generally disregarded their meandering nature. Here, we use idealized simulations to examine the sensitivity of cyclone development to SST meanders of varying size. Each crossing from the cold to the warm side of a meander locally enhances moisture supply into the troposphere, triggering peaks in diabatic heating a few hours later. This, in turn, amplifies the conversion from eddy potential to kinetic energy throughout the troposphere within hours. Both the size and phase of meanders relative to the cyclone modulate this energetic response. Such results reveal that not only the SST gradient but also the SST front geometry affect the life cycle of extratropical cyclones.

Plain Language Summary Extratropical cyclones are large atmospheric systems, about 1,000 km across, that last a few days and strongly influence weather at mid-latitudes. These cyclones often develop over the western parts of ocean basins, above major ocean currents such as the Gulf Stream in the Atlantic or the Kuroshio in the Pacific. These ocean currents are known to intensify extratropical cyclones by supplying moisture to the atmosphere through surface evaporation, which contributes to cloud formation and precipitation. They often form meanders with high sea surface temperature contrasts, which may affect the cyclone life cycle. Using a weather forecast model in an idealized setting, we show that when a cyclone passes over the warm side of a meander, moisture and precipitation increase, strengthening the cyclone within hours. The size of meanders regulates the magnitude of this atmospheric response. Ocean meanders can also shift the timing of cyclone intensification by tens of hours, highlighting the rapid response of extratropical cyclones to ocean temperature contrasts.

1. Introduction

Extratropical cyclones, also called mid-latitude storms, tend to form over western boundary currents (WBCs) such as the Kuroshio-Oyashio Extension (Shaw et al., 2016). WBCs are characterized by strong meridional sea surface temperature (SST) gradients extending over thousands of kilometers. These SST fronts help maintain strong low-level baroclinicity, that is, strong horizontal temperature gradients of the mean atmospheric flow, through surface sensible heat fluxes, thereby anchoring storm tracks (Brayshaw et al., 2008; Deremble et al., 2012; Nakamura et al., 2004). In addition, WBCs act as major sources of atmospheric moisture via surface latent heat flux, which modulates diabatic heating associated with cloud formation and precipitation within cyclones (Demirdjian et al., 2022; Hirata et al., 2015; Sheldon et al., 2017). As a result, SST fronts contribute to the intensification of extratropical cyclones over several days through both baroclinic and diabatic pathways, acting as key sources of eddy kinetic energy (Kirshbaum et al., 2018; Tierney et al., 2018). Integrated over time, cyclone-WBC interaction is noticeable in climatological data, with convective activity and precipitation patterns consistently localized above SST fronts (Larson et al., 2024; Minobe et al., 2008; Vannière et al., 2017), emphasizing the major role of WBCs in driving weather and climate at mid-latitudes. In addition to SST fronts, mesoscale SST anomalies (with horizontal scales of ∼200 km) modulate mid-latitude diabatic heating, thereby influencing storm tracks (Grist et al., 2021; Joyce et al., 2009; Zhang et al., 2019) and the mean atmospheric circulation (Foussard et al., 2019; Ma et al., 2017; O'Reilly & Czaja, 2015; Szunyogh et al., 2021).

Regarding individual cyclone developments, several studies have investigated their sensitivity to the characteristics of the underlying SST front in baroclinic lifecycle experiments or case studies. A uniform increase in SST leads to deeper surface cyclones, primarily due to enhanced diabatic heating (Booth et al., 2012; Bui &

19448007, 2026, 9, Downloaded from https://agupubs.onlinelibrary.wiley.com/doi/10.1029/2025GL121211 by Ecole Normale Supérieure de Paris, Wiley Online Library on [04/05/2026]. See the Terms and Conditions (https://onlinelibrary.wiley.com/terms-and-conditions) on Wiley Online Library for rules of use; OA articles are governed by the applicable Creative Commons License

Spengler, 2021). Likewise, an increased meridional SST gradient or a poleward-shifted SST front modifies the SST encountered during cyclogenesis, promoting more explosive development (Bui & Spengler, 2021; de Vries et al., 2019) and changes in atmospheric frontal frequency (Hirata et al., 2019; Parfitt et al., 2016). Thus far, most sensitivity experiments of this kind have focused on zonally-symmetric characteristics of SST fronts. However, WBCs and their extensions can form meanders with typical scales of a few hundred kilometers, potentially persisting over months (Kelly et al., 2010; Qiu et al., 2014). Comparing different regimes of the Kuroshio Extension characterized by either large-meander or straight paths, Nakamura et al. (2012) and Hayasaki et al. (2013) showed that meanders affect surface latent heat fluxes, cyclone intensification, and the meridional shift of cyclone tracks in the climatology. Although these studies emphasized the impact of SST meanders, the underlying mechanisms remain unclear. Here, we address this knowledge gap with idealized simulations of a cyclonic life cycle. Sensitivity experiments are conducted with the Weather Research and Forecasting (WRF) model, in which the atmosphere is forced by different types of ocean meanders. Using an energy budget, we examine how the presence of meanders influences the eddy kinetic energy of the cyclone through baroclinic and diabatic pathways.

2. Methods and Experiment Design

2.1. Model and Initial Conditions

Simulations are performed with the WRF regional model version 4.3.3 (Skamarock et al., 2019), with physical parameterizations for surface fluxes (Jiménez et al., 2012), planetary boundary layer turbulence (Mellor & Yamada, 1982), microphysics (Chen & Sun, 2002) and cumulus (Kain, 2004). No radiative model is used. Experiments are conducted on the f-plane (at 45 °N), in a zonally periodic channel of size 16,000 km by 6,000 km in the zonal (x) and meridional (y) directions, respectively. In the vertical, the domain extends from the surface to a height of 25 km. Simulations are run over a 5-day period with a horizontal resolution of 20 km and with 61 vertical layers stretched close to the surface (15 layers below 1 km).

The initial atmospheric state is adapted from Bui and Spengler (2021) and consists of a zonally symmetric jet and a cyclonic perturbation, identical across all experiments. The thermal wind balance is imposed to fully determine the initial state from prescribed temperature, pressure, and wind profiles (Plougonven & Zeitlin, 2009). The zonal wind speed of the baroclinic jet is about 5 m s^{-1} at the surface and reaches 50 m s^{-1} at the tropopause ($\sim$8 km height). The cyclonic anomaly radius is 500 km and corresponds to a maximum wind anomaly of 5 m s^{-1} at the surface (Figure 1). A detailed description of the experiment design is given in Supporting Information S1.

In the control (CTL) experiment, the SST distribution corresponds to a large-scale and zonally symmetric ocean front, with a maximum SST gradient of 3°C per 100 km centered at $y = 0$ (Figure 1a). To investigate the role of SST geometry, we introduce sinusoidal SST fronts extending 4,000 km zonally in two additional experiments, M5 and M10, with characteristic sizes of 500 km and 1,000 km, respectively (Figures 1b and 1c). The SST is fixed in time in all the experiments. The meanders are located 1,000 km downstream (east) of the initial cyclonic perturbation, allowing time for the atmosphere to spin up before the cyclone interacts with the ocean meanders (Figure 1). The maximum meridional SST gradient in M5 and M10 is identical to that in CTL (3 °C per 100 km), ensuring that differences in the cyclone life cycle should come from differences in the geometry of the SST front.

2.2. Diagnostics and Energy Budget

The evolution of cyclone intensity is analyzed using both sea level pressure (SLP) diagnostics and an energy budget along its trajectory. Here, the cyclone center is defined as the location of the minimum in SLP zonal anomaly (Figure 1), while surface intensity is the sea level pressure at the cyclone center, denoted SLP_c herein. We define the maximum intensification as the time of the most rapid SLP_c decrease, and the maximum intensity as the time of minimum SLP_c. Additionally, we examine the eddy available potential energy (A_E) and eddy kinetic energy (K_E) budgets associated with the cyclone (Bui & Spengler, 2021; Lorenz, 1955; Moore & Montgomery, 2005).

Before introducing these variables, we define different notations for averages, anomalies and vertically integrated quantities. For any variable X, we note $[X]$ its zonal average and $\overline{X}$ its horizontal mean over the entire domain. With these notations, $X^* = X - [X]$ stands for the zonal anomaly and $X' = X - \overline{X}$ for the horizontal anomaly. The cyclone domain is defined as the 2,000 km × 2,000 km box centered on the cyclone (Figure 1a). $\overline{X}^{cyc}$ is then

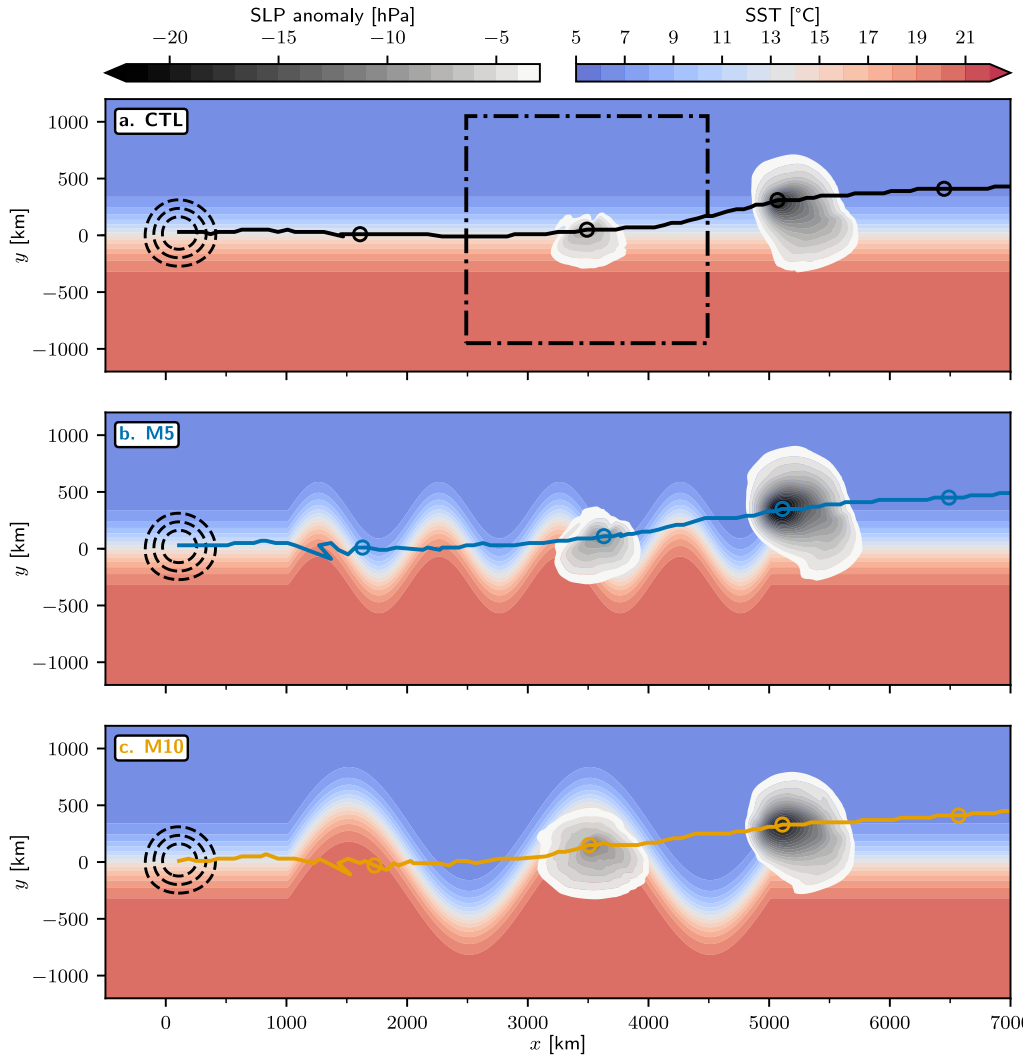

Figure 1. Cyclone development over ocean meanders of varying size. (a) CTL, (b) M5 and (c) M10 experiments. Initial cyclonic perturbation, 1 hr after the start of the simulations, represented by black dashed contours of sea level pressure zonal anomaly (−1.5, −1, and −0.5 hPa). Cyclone trajectory (solid line) marked every 24 hr with circles, sea level pressure anomaly at 48 and 72 hr (gray shading) and SST (color shading). In panel (a), the dash-dotted square represents the cyclone domain at 48 hr for CTL.

the horizontal mean of X over the cyclone domain and $\{X\}_{\text{cyc}}$ its density-weighted vertical integral over the troposphere (from 950 to 100 hPa):

$$\{X\}_{\text{cyc}} = \int_{100\text{ hPa}}^{950\text{ hPa}} \overline{X}^{\text{cyc}} \, \frac{dp}{g} \tag{1}$$

With these notations, A_E and K_E can be written as:

$$A_E = \left\{ g \frac{T^{*2}}{2\overline{\sigma}} \right\}_{\text{cyc}} \tag{2}$$

$$K_E = \left\{ \frac{u^{*2} + v^{*2}}{2} \right\}_{\text{cyc}} \tag{3}$$

19448007, 2026, 9, Downloaded from https://agupubs.onlinelibrary.wiley.com/doi/10.1029/2025GL121211 by Ecole Normale Supérieure de Paris, Wiley Online Library on [04/05/2026]. See the Terms and Conditions (https://onlinelibrary.wiley.com/terms-and-conditions) on Wiley Online Library for rules of use; OA articles are governed by the applicable Creative Commons License

where $\overline{\sigma}$ is the horizontally averaged static stability:

$$\overline{\sigma} = g\left(\frac{\overline{T}}{c_p} - \frac{p}{R_d}\frac{\partial \overline{T}}{\partial p}\right) \tag{4}$$

The budgets of A_E and K_E are then expressed as:

$$\frac{\partial}{\partial t}A_E = C_A + G_E - C_E + R_{A_E} \tag{5}$$

$$\frac{\partial}{\partial t}K_E = C_E + R_{K_E} \tag{6}$$

where C_A is the baroclinic production, G_E the diabatic production and C_E the conversion from A_E to K_E. R_{A_E} is a residual term coming from numerical approximations, dissipation, and lateral fluxes of A_E through the open boundaries of the cyclone domain. R_{K_E} encompasses barotropic effects (surface friction or exchanges with the mean flow) and ageostrophic geopotential fluxes (Orlanski & Sheldon, 1995). Here, we focus on the following terms:

$$C_A = \left\{-g\frac{T^*}{\overline{\sigma}}\left(v^*\frac{\partial}{\partial y} + \omega^*\frac{\partial}{\partial p}\right)[T]'\right\}_{\text{cyc}} \tag{7}$$

$$G_E = \left\{g\frac{T^*}{\overline{\sigma}}\frac{Q^*}{c_p}\right\}_{\text{cyc}} \tag{8}$$

$$C_E = \left\{-R_d\frac{T^*\omega^*}{p}\right\}_{\text{cyc}} \tag{9}$$

where the diabatic heating (Q) is the sum of the heating associated with the microphysics, cumulus, and planetary boundary layer parameterizations.

We also define non-integrated quantities that provide insights into the horizontal and vertical distributions of the processes at play. The eddy kinetic energy and diabatic production per unit mass are

$$k_e = \frac{u^{*2} + v^{*2}}{2}, \quad g_e = \frac{g\,T^*Q^*}{\overline{\sigma}c_p}, \tag{10}$$

so that $K_E = \{k_e\}_{\text{cyc}}$ and $G_E = \{g_e\}_{\text{cyc}}$. Finally, we define the vertical water vapor flux in pressure coordinates as $F_v = -\omega q_v/g$, where q_v is the water vapor mixing ratio.

To ensure the accuracy of the A_E budget (Equation 5), we evaluated R_{A_E} over the entire domain, that is, using $\overline{X}$ instead of $\overline{X}^{\text{cyc}}$ in Equation 1 when computing the budget. R_{A_E} was found to be five times smaller in absolute value than the other terms (not shown). When restricting the budget to the cyclone domain, R_{A_E} is found to be always negative and twice smaller than the other terms during the first 60 hr. At later times, it increases in magnitude, which may be due to lateral fluxes radiating energy outward from the cyclone domain to the surrounding environment, resulting in the development of upstream and downstream cyclones (Figure S3 in Supporting Information S1). These structures are not the focus of our analysis.

3. Results

3.1. Time Evolution of Cyclone Energetics

The surface cyclone in CTL travels approximately 5,000 km eastward during the first 72 hr due to advection by the zonal jet and 500 km northward (Figure 1a). It keeps intensifying until 80 hr, with a maximum intensification reached at 68 hr and a maximum intensity at 80 hr, and then decays (Figure 2a). K_E temporal evolution aligns with

19448007, 2026, 9, Downloaded from https://agupubs.onlinelibrary.wiley.com/doi/10.1029/2025GL121211 by Ecole Normale Supérieure de Paris, Wiley Online Library on [04/05/2026]. See the Terms and Conditions (https://onlinelibrary.wiley.com/terms-and-conditions) on Wiley Online Library for rules of use; OA articles are governed by the applicable Creative Commons License

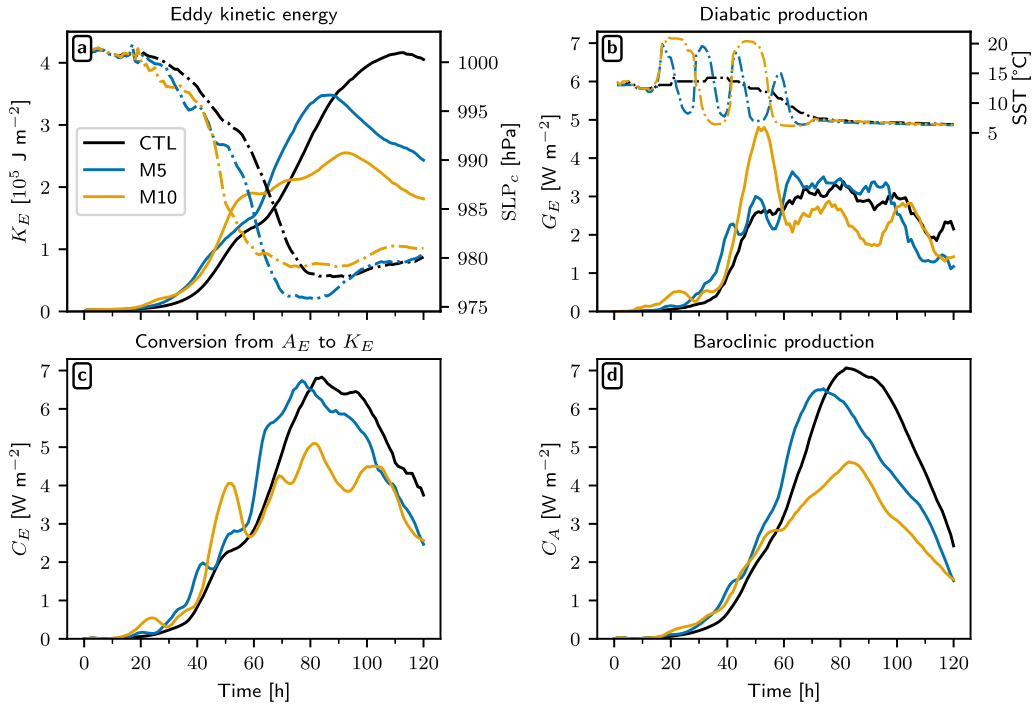

Figure 2. Cyclone energetic response to ocean meanders. (a) Eddy kinetic energy (K_E, solid lines) and sea level pressure at the cyclone center (SLP$_c$, dash-dotted lines). (b) Diabatic production (G_E, solid lines) of eddy available potential energy (A_E) and SST underneath the cyclone center (dash-dotted lines). (c) Conversion from A_E to K_E (C_E, solid lines). (d) Baroclinic production of A_E (C_A, solid lines). K_E, G_E, C_E and C_A are vertically integrated and horizontally averaged quantities over the cyclone domain (see Methods). Black, blue and orange lines correspond to CTL, M5 and M10 experiments, respectively.

that of SLP$_c$, but with a maximum reached at 110 hr after the SLP$_c$ minimum (Figure 2a). During the deepening phase, R_{K_E} remains smaller than C_E in absolute value (not shown) and the increase in K_E is mostly explained by positive C_E (see Equation 6 and Figure 2c). After 110 hr, although C_E remains positive in CTL, K_E starts decreasing due to negative R_{K_E} through surface friction and ageostrophic geopotential fluxes radiating energy outside the cyclone domain. Two other terms affect the A_E budget (Equation 5): the diabatic production (G_E, Figure 2b), which is related to water condensation, and the baroclinic production (C_A, Figure 2d), which is the extraction of potential energy from the mean flow. The overall evolution of C_E in CTL is similar to that of C_A, with an increasing phase during the first 80 hr, followed by a decreasing phase (Figures 2c and 2d). On the other hand, G_E sharply increases after 30 hr and plateaus at 50 hr in CTL with an amplitude similar to C_E up to 50 hr. In these experiments, both baroclinic and diabatic productions of A_E contribute to the cyclone development, as they are sources of K_E via the conversion term, C_E.

Surface cyclones in M5 and M10 develop over ocean meanders for approximately two days, from 20 to 70 hr (Figures 1b and 1c). Their trajectories are similar, with small differences of about 100 km across experiments. As in CTL, the M5 and M10 cyclones deepen and then decay, but with a notable difference in the timing of maximum intensification: it occurs at 60 hr in M5 and at 48 hr in M10, that is, 8 and 20 hr earlier than CTL, respectively (Figure 2a). The most intensified cyclone corresponds to the M5 experiment at approximately 72 hr, as reflected in both the spatial field of SLP anomaly (Figure 1) and the evolution of SLP$_c$ (Figure 2a). Similar differences are also observed in K_E until 90 hr, after which K_E in CTL exceeds that in M5, despite M5 having a lower SLP$_c$ (Figure 2a). This is because K_E accounts for all the troposphere, while SLP$_c$ reflects only surface intensity. Overall, ocean meanders affect cyclone intensification, in terms of both SLP$_c$ and K_E.

C_E is found to be greater in M5 and M10 than in CTL during the first 60 hr (Figure 2c), accounting for differences in intensification across experiments. As C_A is similar between M5 and M10 (Figure 2d), the latter quantity does not explain the differences between M5 and M10 in C_E, with a higher C_E for M10 at 22 and 52 hr and a higher C_E for M5 at 40 hr (Figure 2c). In fact, it can be attributed to pronounced peaks in G_E that occur at different times for M5 and M10 (Figure 2b). In other words, the cyclone in M5 and M10 intensifies earlier compared to CTL due to

19448007, 2026, 9, Downloaded from https://agupubs.onlinelibrary.wiley.com/doi/10.1029/2025GL121211 by Ecole Normale Supérieure de Paris, Wiley Online Library on [04/05/2026]. See the Terms and Conditions (https://onlinelibrary.wiley.com/terms-and-conditions) on Wiley Online Library for rules of use; OA articles are governed by the applicable Creative Commons License

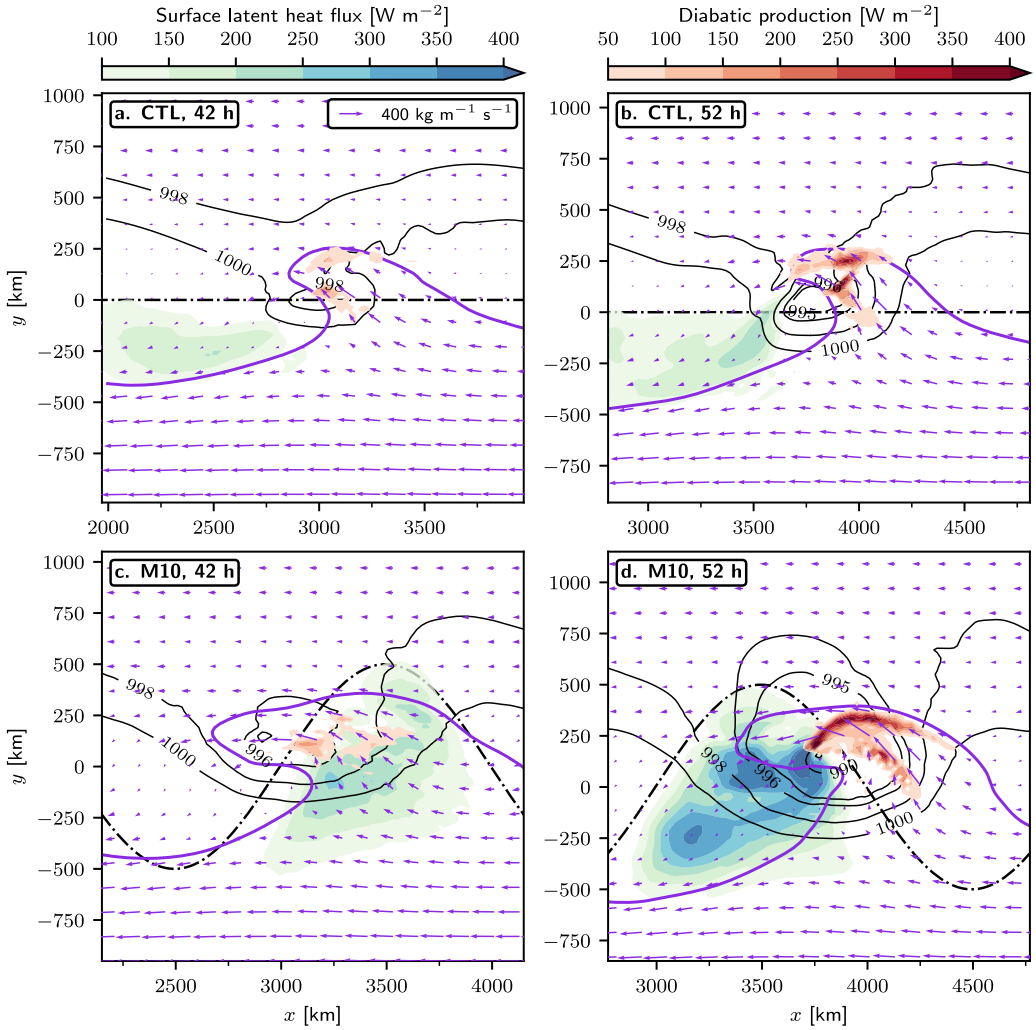

Figure 3. Moisture supply and diabatic production over the warm side of a meander. (a, b) CTL and (c, d) M10 at (a, c) 42 hr and (b, d) 52 hr. Panels are centered on the cyclone center. Surface latent heat flux (blue-green shading), vertically integrated diabatic production ($\int_{100\ \mathrm{hPa}}^{950\ \mathrm{hPa}} g_e dp/g$, red shading), sea level pressure (black solid contours, in hPa) and vertically integrated horizontal moisture flux relative to the cyclone (purple arrows). The SST front is denoted by a black dash-dotted line. The thick purple contour represents a vertically integrated water vapor content of 14 kg m^{-2}.

an enhanced diabatic production driven by ocean meanders. In addition, this diabatic response is modulated by the size of the meanders, as shown by the differences in G_E between M5 and M10 (Figure 2b). In the following, we focus primarily on these diabatic processes.

3.2. Modulation of Diabatic Heating by Ocean Meanders

Peaks in G_E occur at 22 and 52 hr in M10, and at 41 hr, 50 hr, and 62 hr in M5, a few hours after the cyclone center passes over the warm side of the ocean meanders, as shown by the corresponding variation of G_E and the underlying SST in Figure 2b. For example, in experiment M10, G_E reaches its maximum at 52 hr, after the cyclone passed over the warm side of a meander at 47 hr. The magnitude of G_E associated with this peak is 4.7 W m^{-2}, while the value in CTL is 2.6 W m^{-2} at the same instant, suggesting that ocean meanders can strongly increase the diabatic production compared to a zonal SST front.

The impact of the warm side of a meander on the moisture supply and the diabatic production is presented in Figure 3 through the comparison between CTL and M10. The thick purple contour delineates the warm sector (southeast) from the cold sector (northwest) of the cyclone. The warm conveyor belt (WCB) above the warm

19448007, 2026, 9, Downloaded from https://agupubs.onlinelibrary.wiley.com/doi/10.1029/2025GL121211 by Ecole Normale Supérieure de Paris, Wiley Online Library on [04/05/2026]. See the Terms and Conditions (https://onlinelibrary.wiley.com/terms-and-conditions) on Wiley Online Library for rules of use; OA articles are governed by the applicable Creative Commons License

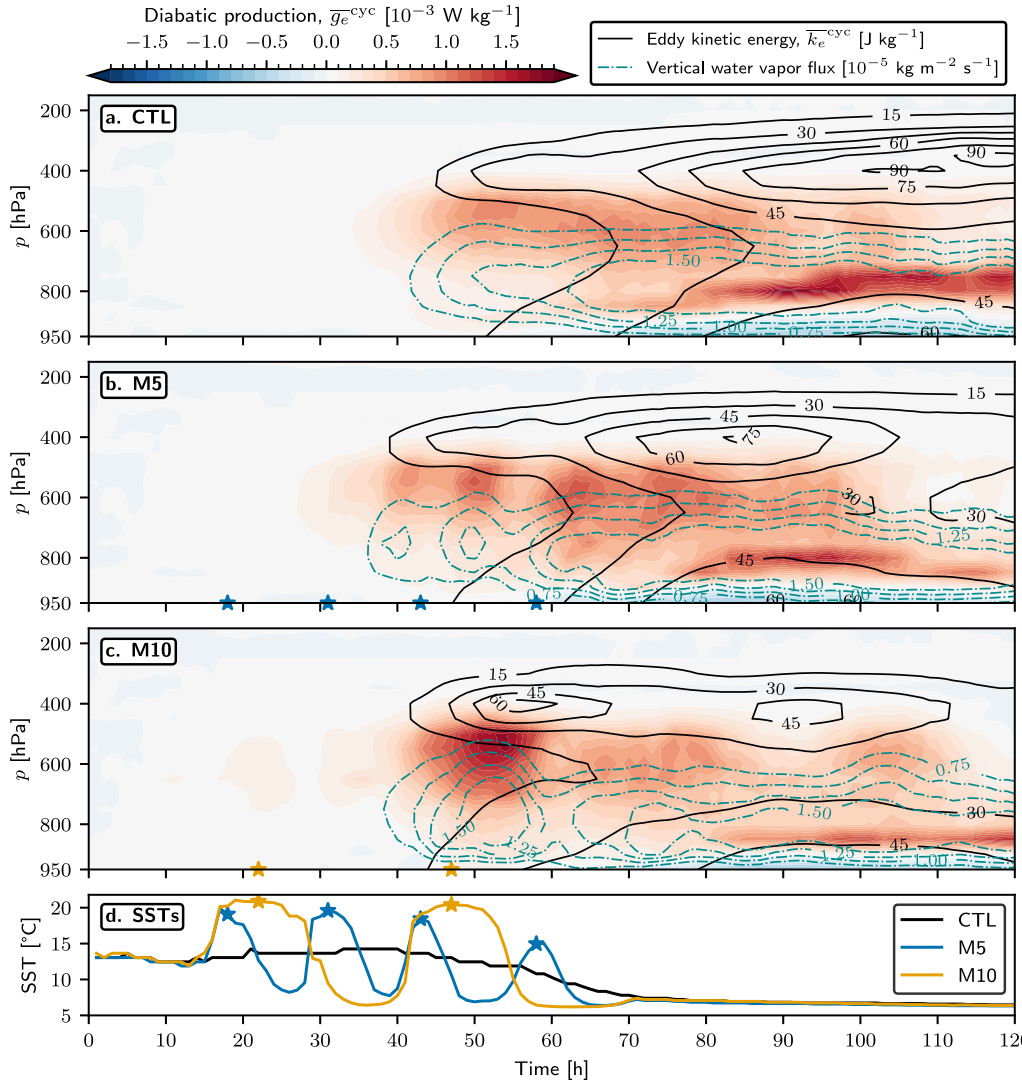

Figure 4. Hovmöller diagram and deep tropospheric response. (a–c) Diabatic production ($\overline{g_e}^{cyc}$, shading), eddy kinetic energy ($\overline{k_e}^{cyc}$, black contours), and vertical flux of water vapor ($\overline{F_v}^{cyc}$, cyan dash-dotted contours) averaged over the cyclone domain. Panels (a) CTL, (b) M5 and (c) M10 experiments. (d) SST underneath the cyclone center for CTL (black), M5 (blue), and M10 (orange). In panels (b–d), stars indicate times when the cyclone center is located above the warm sides of the meanders.

sector carries warm and moist air masses upward and northward, as shown by purple arrows of moisture flux, resulting in pronounced G_E associated with water condensation (Figures 3a and 3b). On the other hand, the dry intrusion above the cold sector carries cold and dry air masses downward and southward (Browning, 1997; Dacre et al., 2019), creating a high air-sea contrast above the southern side of the SST front in CTL, as shown by surface latent heat flux reaching 200 W m^{-2} (Figures 3a and 3b). In contrast to CTL, at 42 hr, the warm sector of the cyclone in M10 is located above the warm side of an ocean meander, producing high surface latent heat fluxes of up to 250 W m^{-2} (Figure 3c). This subsequently increases the moisture flux and G_E within the WCB at 52 hr in M10 compared to CTL (Figures 3b and 3d), explaining the G_E peak observed at 52 hr (Figure 2b).

The vertical extension of the diabatic response to ocean meanders is presented in Figure 4. In the CTL experiment, a gradual increase in vertical water vapor flux over time is observed in layers below 550 hPa (∼5 km height) until 70 hr, corresponding to the vertical advection of moisture within the WCB, which induces a gradual enhancement in $\overline{g_e}^{cyc}$ at 550 hPa (Figure 4a). In turn, $\overline{k_e}^{cyc}$ of the surface cyclone (below the 650 hPa level) increases, as well as that of the upper-level anomalies (above 650 hPa). In contrast, vertical water vapor flux in M10 reaches a distinct maximum at 52 hr exceeding 1.5 kg m^{-2} s^{-1} at 750 hPa (∼3 km height), which leads to the $\overline{g_e}^{cyc}$ peak at 550 hPa

19448007, 2026, 9, Downloaded from https://agupubs.onlinelibrary.wiley.com/doi/10.1029/2025GL121211 by Ecole Normale Supérieure de Paris, Wiley Online Library on [04/05/2026]. See the Terms and Conditions (https://onlinelibrary.wiley.com/terms-and-conditions) on Wiley Online Library for rules of use; OA articles are governed by the applicable Creative Commons License

19448007, 2026, 9, Downloaded from https://agupubs.onlinelibrary.wiley.com/doi/10.1029/2025GL121211 by Ecole Normale Supérieure de Paris, Wiley Online Library on [04/05/2026]. See the Terms and Conditions (https://onlinelibrary.wiley.com/terms-and-conditions) on Wiley Online Library for rules of use; OA articles are governed by the applicable Creative Commons License

(Figure 4c). A conspicuous $\overline{k_e}^{cyc}$ response is seen in M10 at upper-levels, where $\overline{k_e}^{cyc}$ at 400 hPa increases from 15 J kg^{-1} at 42 hr to 60 J kg^{-1} at 52 hr (Figure 4c). The delay between the time when the cyclone is centered over the warm side of the meander (at 47 hr) and the subsequent peak in $\overline{g_e}^{cyc}$ (at 52 hr) is approximately 5–10 hr (Figures 4c and 4d), which likely corresponds to the ascent time for surface air parcels to reach 5 km within the WCB (Bui & Spengler, 2021; Demirdjian et al., 2022). These results emphasize that the diabatic response to ocean meanders extends throughout the troposphere, impacting the eddy kinetic energy of surface and upper-level anomalies.

The same diabatic mechanism is observed in M5, with three different $\overline{g_e}^{cyc}$ peaks when the cyclone passes over the warm sides of ocean meanders (Figure 4b). Due to smaller meanders in size compared to M10, less water vapor is advected within the WCB for each of them, leading to weaker $\overline{g_e}^{cyc}$ maxima (Figure 4b). However, the cumulative effect of small meanders sustains the G_E increase in M5 compared to M10, leading to a higher K_E maximum and a lower SLP$_c$ minimum (Figure 2a). In fact, while the large ocean meanders drive the earlier cyclone intensification in M10 compared to M5 or CTL, they also cause an earlier decay after 60 hr (Figure 2a). In the following, we discuss these later stages of development.

3.3. Later Stages of Development

At 60 hr, the M10 cyclone passes over the cold side of the meander (Figure 4d), which is 4 °C cooler than the SST in the other experiments. As a result, the surface latent heat flux strongly decreases leading to less water vapor advected by the WCB and a drop in G_E at 60 hr (Figures 2b and 4c). After 60 hr, not only G_E drops in M10, but C_A also experiences a slower increase than in M5 and CTL (Figure 2d). It suggests that both G_E and C_A inhibition participate in the early cyclone decay in M10.

To better understand the weak growth of C_A in M10 during the later stages of development, we examine a simplified expression of C_A determined from Equation 7:

$$C_A \approx \left\{ T^* v^* \sqrt{\frac{g}{\overline{\sigma}}} \sigma_E \right\}_{\text{cyc}} \tag{11}$$

where we neglected the vertical term. In Equation 11, $T^* v^* \sqrt{g/\overline{\sigma}}$ is the meridional eddy heat flux and σ_E is the baroclinicity of the mean flow, given that $\partial_y [T]' = \partial_y [T] - \partial_y \left[\overline{T}\right] = \partial_y [T]$:

$$\sigma_E = -\sqrt{\frac{g}{\overline{\sigma}}} \frac{\partial [T]}{\partial y} \tag{12}$$

For each experiment, we compute the Eady growth rate as $0.31\,\overline{\sigma_E}^{cyc}$ at 850 hPa, that is, the low-level baroclinicity averaged over the cyclone domain. It remains relatively constant in time and across experiments, with a value around 0.62 day^{-1} (not shown). The evolution of C_A is indeed largely driven by eddy heat flux, with a Pearson correlation coefficient greater than 0.95 between C_A and $\left\{ T^* v^* \sqrt{g/\overline{\sigma}} \right\}_{\text{cyc}}$. Thus, a possible explanation for the weak growth of C_A in M10 after 60 hr is that the cold and warm sectors of the cyclone are out of phase with the warm and cold sides of the ocean meanders (Figure 3d). Because the atmospheric cold sector in M10 is above the warm side of the ocean meander at 52 hr, it is warmed by high fluxes reaching 400 W m^{-2} (Figure 3d), while the warm sector is cooled. This should decrease the temperature anomaly in absolute value ($|T^*|$) in both the warm and cold sectors, thereby reducing the eddy heat flux ($T^* v^*$) and C_A afterward (Figure 2d).

Regarding M5, G_E and C_A keep increasing until 70 hr, when the cyclone passes over the last warm side of the meanders (Figures 2b and 2d). In CTL, C_A continues to increase the longest and attains the highest value across the experiment (Figure 2d), which might explain why the largest K_E maximum is observed in CTL after 90 hr (Figure 2a). This elevated K_E actually corresponds to strong upper-level anomalies, with $\overline{k_e}^{cyc}$ reaching 90 J kg^{-1} at 400 hPa compared to 45 J kg^{-1} in M5 (Figures 4a and 4b). In contrast, both CTL and M5 exhibit similar $\overline{k_e}^{cyc}$ values about 50 J kg^{-1} below 800 hPa (Figures 4a and 4b), in agreement with similar SLP$_c$ values after 90 hr (Figure 2a). Overall, these findings indicate that the modulation of C_A by ocean meanders influences K_E during the later stages of development, especially at upper levels. Large meanders (M10) lead to a greater inhibition of

C_A than small meanders (M5) or than a zonal SST front (CTL). Despite that, the decrease in K_E is also driven by a negative R_{K_E} that exceeds C_E in absolute value (not shown). This suggests that ocean meanders also affect the barotropic conversion to the mean flow, as well as the downstream and upstream development of perturbations through ageostrophic geopotential fluxes.

4. Conclusions and Discussion

In this study, we present mechanisms through which ocean meanders modulate extratropical cyclone energetics. Each time the cyclone passes over the warm side of a meander, surface latent heat fluxes strongly increase, leading to enhanced moisture supply within the warm conveyor belt of the cyclone. This triggers intense diabatic heating events during the cyclone deepening phase, which in turn amplify both surface and upper-level anomalies within hours. Large meanders (∼1,000 km) drive greater diabatic events, whereas the combined influence of small meanders (∼500 km) can sustain elevated diabatic production for longer periods of time. This diabatic response driven by ocean meanders leads to surface intensity differences in terms of sea level pressure compared to a zonal SST front. On the other hand, we observe the cold side of a large meander reducing the moisture supply and the baroclinic production during the later stages of development, which contribute to earlier cyclone decay. As such, extratropical cyclones strongly interact with ocean meanders, which affects their life cycle through both diabatic and baroclinic pathways.

We found similar results in sensitivity experiments with the initial cyclonic perturbation shifted 100 km to the north or to the south (Figure S4 in Supporting Information S1), ensuring the robustness of our analysis. We also conducted experiments with SST configurations opposite to those of M5 and M10, in which cold and warm SST anomalies associated with the meanders are reversed (Figure S5 in Supporting Information S1). The same mechanisms are observed, such as peaks in G_E, but they occur at different times and magnitudes, which in turn have a different impact on K_E. This indicates that the energetic response of extratropical cyclones through these mechanisms is modulated not only by the size of meanders but also by their phase relative to the cyclone development.

While baroclinic life cycle experiments allow us to identify a clear diabatic response of cyclones to ocean meanders, the atmospheric variability on a case-by-case basis in the reanalysis might hide this effect. However, previous studies have shown a significant diabatic response of storm tracks to ocean mesoscale structures (Foussard et al., 2019; Ma et al., 2017). It has also been shown that cold SST anomalies associated with the large meander of the Kuroshio have a role in reducing cyclone intensification in the climatology (Hayasaki et al., 2013; Nakamura et al., 2012). We suspect that the latter occurs through similar mechanisms to those observed in experiment M10, where reduced diabatic and baroclinic productions lead to an early cyclone decay. Thus, when integrated over many cyclones propagating along western boundary currents, the effect of ocean meanders we observe may be significant enough to influence storm tracks over extended periods. Overall, this interpretation is consistent with the strong sensitivity of storm-track activity to ocean resolution reported in general circulation model studies (Chang et al., 2020; Grist et al., 2021).

Our study focuses on meanders of several hundred kilometers in size due to the highly idealized nature of the SST fields considered. In reality, western boundary currents exhibit much finer and more complex structures, including mesoscale eddies and submesoscale fronts, which must be considered to accurately represent atmospheric circulation in weather and climate models (Czaja et al., 2019; Seo et al., 2023). Notably, Vivant et al. (2025) showed that ocean submesoscale fronts can locally induce diabatic heating within cyclones. Such interactions, along with atmosphere–ocean coupling, are excluded in our framework, which constitutes a limitation. Nevertheless, our results demonstrate that extratropical cyclones respond to diabatic forcing from SST anomalies within just a few hours.

Conflict of Interest

The authors declare no conflicts of interest relevant to this study.

19448007, 2026, 9, Downloaded from https://agupubs.onlinelibrary.wiley.com/doi/10.1029/2025GL121211 by Ecole Normale Supérieure de Paris, Wiley Online Library on [04/05/2026]. See the Terms and Conditions (https://onlinelibrary.wiley.com/terms-and-conditions) on Wiley Online Library for rules of use; OA articles are governed by the applicable Creative Commons License

Availability Statement

Data and codes to reproduce the figures are available from Vivant and Lapeyre (2026a, 2026b), respectively. A description of WRF v4.3.3 and the source code is provided by Skamarock et al. (2019). Details about the configuration and parameters used to run the model, as well as necessary information for conducting the analysis, can be found in Methods and in Supporting Information S1.

Acknowledgments
The authors acknowledge two anonymous reviewers, who helped improve the manuscript. This work is a contribution to the projects I-CASCADE and POSEIDON funded by the French CNES TOSCA program. This work was granted access to the HPC resources of IDRIS under the allocation AD010106852R2 made by GENCI (Grand Equipement National de Calcul Intensif). F.V. is supported by a CDSN doctoral studentship through ENS Paris-Saclay.

References

Booth, J. F., Thompson, L., Patoux, J., & Kelly, K. A. (2012). Sensitivity of midlatitude storm intensification to perturbations in the sea surface temperature near the Gulf Stream. *Monthly Weather Review*, *140*(4), 1241–1256. https://doi.org/10.1175/mwr-d-11-00195.1

Brayshaw, D. J., Hoskins, B., & Blackburn, M. (2008). The storm-track response to idealized SST perturbations in an aquaplanet GCM. *Journal of the Atmospheric Sciences*, *65*(9), 2842–2860. https://doi.org/10.1175/2008jas2657.1

Browning, K. (1997). The dry intrusion perspective of extra-tropical cyclone development. *Meteorological Applications*, *4*(4), 317–324. https://doi.org/10.1017/s1350482797000613

Bui, H., & Spengler, T. (2021). On the influence of sea surface temperature distributions on the development of extratropical cyclones. *Journal of the Atmospheric Sciences*, *78*(4), 1173–1188. https://doi.org/10.1175/jas-d-20-0137.1

Chang, P., Zhang, S., Danabasoglu, G., Yeager, S. G., Fu, H., Wang, H., et al. (2020). An unprecedented set of high-resolution Earth system simulations for understanding multiscale interactions in climate variability and change. *Journal of Advances in Modeling Earth Systems*, *12*(12), e2020MS002298. https://doi.org/10.1029/2020ms002298

Chen, S.-H., & Sun, W.-Y. (2002). A one-dimensional time dependent cloud model. *Journal of the Meteorological Society of Japan. Series II*, *80*(1), 99–118. https://doi.org/10.2151/jmsj.80.99

Czaja, A., Frankignoul, C., Minobe, S., & Vannière, B. (2019). Simulating the midlatitude atmospheric circulation: What might we gain from high-resolution modeling of air-sea interactions? *Current Climate Change Reports*, *5*(4), 390–406. https://doi.org/10.1007/s40641-019-00148-5

Dacre, H. F., Martinez-Alvarado, O., & Mbengue, C. O. (2019). Linking atmospheric rivers and warm conveyor belt airflows. *Journal of Hydrometeorology*, *20*(6), 1183–1196. https://doi.org/10.1175/jhm-d-18-0175.1

Demirdjian, R., Doyle, J. D., Finocchio, P. M., & Reynolds, C. A. (2022). On the influence of surface latent heat fluxes on idealized extratropical cyclones. *Journal of the Atmospheric Sciences*, *79*(9), 2229–2242. https://doi.org/10.1175/jas-d-22-0035.1

Deremble, B., Lapeyre, G., & Ghil, M. (2012). Atmospheric dynamics triggered by an oceanic SST front in a moist quasigeostrophic model. *Journal of the Atmospheric Sciences*, *69*(5), 1617–1632. https://doi.org/10.1175/jas-d-11-0288.1

de Vries, H., Scher, S., Haarsma, R., Drijfhout, S., & van Delden, A. (2019). How Gulf-Stream SST-fronts influence Atlantic winter storms: Results from a downscaling experiment with HARMONIE to the role of modified latent heat fluxes and low-level baroclinicity. *Climate Dynamics*, *52*(9), 5899–5909. https://doi.org/10.1007/s00382-018-4486-7

Foussard, A., Lapeyre, G., & Plougonven, R. (2019). Storm track response to oceanic eddies in idealized atmospheric simulations. *Journal of Climate*, *32*(2), 445–463. https://doi.org/10.1175/jcli-d-18-0415.1

Grist, J. P., Josey, S. A., Sinha, B., Catto, J. L., Roberts, M. J., & Coward, A. C. (2021). Future evolution of an eddy rich ocean associated with enhanced east Atlantic storminess in a coupled model projection. *Geophysical Research Letters*, *48*(7), e2021GL092719. https://doi.org/10.1029/2021gl092719

Hayasaki, M., Kawamura, R., Mori, M., & Watanabe, M. (2013). Response of extratropical cyclone activity to the Kuroshio large meander in northern winter. *Geophysical Research Letters*, *40*(11), 2851–2855. https://doi.org/10.1002/grl.50546

Hirata, H., Kawamura, R., Kato, M., & Shinoda, T. (2015). Influential role of moisture supply from the Kuroshio/Kuroshio Extension in the rapid development of an extratropical cyclone. *Monthly Weather Review*, *143*(10), 4126–4144. https://doi.org/10.1175/mwr-d-15-0016.1

Hirata, H., Kawamura, R., Yoshioka, M. K., Nonaka, M., & Tsuboki, K. (2019). Key role of the Kuroshio Current in the formation of frontal structure of an extratropical cyclone associated with heavy precipitation. *Journal of Geophysical Research: Atmospheres*, *124*(12), 6143–6156. https://doi.org/10.1029/2018jd029578

Jiménez, P. A., Dudhia, J., González-Rouco, J. F., Navarro, J., Montávez, J. P., & García-Bustamante, E. (2012). A revised scheme for the WRF surface layer formulation. *Monthly Weather Review*, *140*(3), 898–918. https://doi.org/10.1175/mwr-d-11-00056.1

Joyce, T. M., Kwon, Y.-O., & Yu, L. (2009). On the relationship between synoptic wintertime atmospheric variability and path shifts in the Gulf Stream and the Kuroshio Extension. *Journal of Climate*, *22*(12), 3177–3192. https://doi.org/10.1175/2008jcli2690.1

Kain, J. S. (2004). The Kain–Fritsch convective parameterization: An update. *Journal of Applied Meteorology*, *43*(1), 170–181. https://doi.org/10.1175/1520-0450(2004)043<0170:tkcpau>2.0.co;2

Kelly, K. A., Small, R. J., Samelson, R., Qiu, B., Joyce, T. M., Kwon, Y.-O., & Cronin, M. F. (2010). Western boundary currents and frontal air–sea interaction: Gulf Stream and Kuroshio Extension. *Journal of Climate*, *23*(21), 5644–5667. https://doi.org/10.1175/2010jcli3346.1

Kirshbaum, D., Merlis, T., Gyakum, J., & McTaggart-Cowan, R. (2018). Sensitivity of idealized moist baroclinic waves to environmental temperature and moisture content. *Journal of the Atmospheric Sciences*, *75*(1), 337–360. https://doi.org/10.1175/jas-d-17-0188.1

Larson, J. G., Thompson, D. W., & Hurrell, J. W. (2024). Signature of the western boundary currents in local climate variability. *Nature*, *634*(8035), 862–867. https://doi.org/10.1038/s41586-024-08019-2

Lorenz, E. N. (1955). Available potential energy and the maintenance of the general circulation. *Tellus*, *7*(2), 157–167. https://doi.org/10.3402/tellusa.v7i2.8796

Ma, X., Chang, P., Saravanan, R., Montuoro, R., Nakamura, H., Wu, D., et al. (2017). Importance of resolving Kuroshio front and eddy influence in simulating the North Pacific storm track. *Journal of Climate*, *30*(5), 1861–1880. https://doi.org/10.1175/jcli-d-16-0154.1

Mellor, G. L., & Yamada, T. (1982). Development of a turbulence closure model for geophysical fluid problems. *Reviews of Geophysics*, *20*(4), 851–875. https://doi.org/10.1029/rg020i004p00851

Minobe, S., Kuwano-Yoshida, A., Komori, N., Xie, S.-P., & Small, R. J. (2008). Influence of the Gulf Stream on the troposphere. *Nature*, *452*(7184), 206–209. https://doi.org/10.1038/nature06690

Moore, R. W., & Montgomery, M. T. (2005). Analysis of an idealized, three-dimensional diabatic rossby vortex: A coherent structure of the moist baroclinic atmosphere. *Journal of the Atmospheric Sciences*, *62*(8), 2703–2725. https://doi.org/10.1175/jas3472.1

Nakamura, H., Nishina, A., & Minobe, S. (2012). Response of storm tracks to bimodal Kuroshio path states south of Japan. *Journal of Climate*, *25*(21), 7772–7779. https://doi.org/10.1175/jcli-d-12-00326.1

19448007, 2026, 9, Downloaded from https://agupubs.onlinelibrary.wiley.com/doi/10.1029/2025GL121211 by Ecole Normale Supérieure de Paris, Wiley Online Library on [04/05/2026]. See the Terms and Conditions (https://onlinelibrary.wiley.com/terms-and-conditions) on Wiley Online Library for rules of use; OA articles are governed by the applicable Creative Commons License

Nakamura, H., Sampe, T., Tanimoto, Y., & Shimpo, A. (2004). Observed associations among storm tracks, jet streams and midlatitude oceanic fronts. Earth's climate: The Ocean–Atmosphere Interaction. *Geophysical Monograph Series*, *147*, 329–345.

O'Reilly, C. H., & Czaja, A. (2015). The response of the Pacific storm track and atmospheric circulation to Kuroshio Extension variability. *Quarterly Journal of the Royal Meteorological Society*, *141*(686), 52–66. https://doi.org/10.1002/qj.2334

Orlanski, I., & Sheldon, J. P. (1995). Stages in the energetics of baroclinic systems. *Tellus*, *47*(5), 605–628. https://doi.org/10.3402/tellusa.v47i5.11553

Parfitt, R., Czaja, A., Minobe, S., & Kuwano-Yoshida, A. (2016). The atmospheric frontal response to SST perturbations in the Gulf Stream region. *Geophysical Research Letters*, *43*(5), 2299–2306. https://doi.org/10.1002/2016gl067723

Plougonven, R., & Zeitlin, V. (2009). Nonlinear development of inertial instability in a barotropic shear. *Physics of Fluids*, *21*(10), 106601. https://doi.org/10.1063/1.3242283

Qiu, B., Chen, S., Schneider, N., & Taguchi, B. (2014). A coupled decadal prediction of the dynamic state of the Kuroshio Extension system. *Journal of Climate*, *27*(4), 1751–1764. https://doi.org/10.1175/jcli-d-13-00318.1

Seo, H., O'Neill, L. W., Bourassa, M. A., Czaja, A., Drushka, K., Edson, J. B., et al. (2023). Ocean mesoscale and frontal-scale ocean–atmosphere interactions and influence on large-scale climate: A review. *Journal of Climate*, *36*(7), 1981–2013. https://doi.org/10.1175/jcli-d-21-0982.1

Shaw, T., Baldwin, M., Barnes, E. A., Caballero, R., Garfinkel, C., Hwang, Y.-T., et al. (2016). Storm track processes and the opposing influences of climate change. *Nature Geoscience*, *9*(9), 656–664. https://doi.org/10.1038/ngeo2783

Sheldon, L., Czaja, A., Vannière, B., Morcrette, C., Sohet, B., Casado, M., & Smith, D. (2017). A 'warm path' for Gulf Stream–troposphere interactions. *Tellus A: Dynamic Meteorology and Oceanography*, *69*(1), 1299397. https://doi.org/10.1080/16000870.2017.1299397

Skamarock, W. C., Klemp, J. B., Dudhia, J., Gill, D. O., Liu, Z., Berner, J., et al. (2019). A description of the advanced research WRF model version 4. *National Center for Atmospheric Research*, *145*, 550. https://doi.org/10.5065/1dfh-6p97

Szunyogh, I., Forinash, E., Gyarmati, G., Jia, Y., Chang, P., & Saravanan, R. (2021). Evaluation of a coupled modeling approach for the investigation of the effects of SST mesoscale variability on the atmosphere. *Journal of Advances in Modeling Earth Systems*, *13*(9), e2020MS002412. https://doi.org/10.1029/2020ms002412

Tierney, G., Posselt, D. J., & Booth, J. F. (2018). An examination of extratropical cyclone response to changes in baroclinicity and temperature in an idealized environment. *Climate Dynamics*, *51*(9), 3829–3846. https://doi.org/10.1007/s00382-018-4115-5

Vannière, B., Czaja, A., Dacre, H., & Woollings, T. (2017). A "cold path" for the Gulf Stream–troposphere connection. *Journal of Climate*, *30*(4), 1363–1379. https://doi.org/10.1175/jcli-d-15-0749.1

Vivant, F., & Lapeyre, G. (2026a). Ocean meanders modulate extratropical cyclone energetics - Data [Dataset]. https://doi.org/10.5281/zenodo.18846024

Vivant, F., & Lapeyre, G. (2026b). Ocean meanders modulate extratropical cyclone energetics (v1.0.1) [Software]. https://doi.org/10.5281/zenodo.18861178

Vivant, F., Siegelman, L., Klein, P., Torres, H. S., Menemenlis, D., & Molod, A. M. (2025). Ocean submesoscale fronts induce diabatic heating and convective precipitation within storms. *Communications Earth & Environment*, *6*(1), 69. https://doi.org/10.1038/s43247-025-02002-z

Zhang, X., Ma, X., & Wu, L. (2019). Effect of mesoscale oceanic eddies on extratropical cyclogenesis: A tracking approach. *Journal of Geophysical Research: Atmospheres*, *124*(12), 6411–6422. https://doi.org/10.1029/2019jd030595

References From the Supporting Information

Klemp, J., Dudhia, J., & Hassiotis, A. (2008). An upper gravity-wave absorbing layer for nwp applications. *Monthly Weather Review*, *136*(10), 3987–4004. https://doi.org/10.1175/2008mwr2596.1

19448007, 2026, 9, Downloaded from https://agupubs.onlinelibrary.wiley.com/doi/10.1029/2025GL121211 by Ecole Normale Supérieure de Paris, Wiley Online Library on [04/05/2026]. See the Terms and Conditions (https://onlinelibrary.wiley.com/terms-and-conditions) on Wiley Online Library for rules of use; OA articles are governed by the applicable Creative Commons License

Supporting Information for 'Ocean meanders modulate extratropical cyclone energetics'

Félix Vivant[1]and Guillaume Lapeyre[1]

[1]LMD-IPSL, ENS, PSL Université, Ecole Polytechnique, IP Paris, Sorbonne Université, CNRS, Paris, France

Contents of this file

1. Text S1 to S3
2. Table S1
3. Figures S1 to S5

Introduction

This document describes the model configuration and the prescribed initial conditions for the ocean and the atmosphere.

Text S1: Precision on the WRF configuration and conventions

Simulations use a time step of 100 s, with model outputs stored hourly. A vertical-velocity damping layer, 5 km deep below the model top, is applied to reduce gravity wave reflection (Klemp et al., 2008). In the following, we define the coordinate system such that x, y, and z denote the zonal, meridional, and vertical axes, respectively. The experimental domain spans 16000 km in the x-direction and 6000 km in the y-direction. By convention, the origin $(x, y) = (0, 0)$ is set at the location of the initial cyclonic

perturbation, which is centered meridionally and located 2000 km east of the western boundary of the domain. In this reference frame, the simulation domain is defined as: $(x, y) \in [-2000 \text{ km}, 14000 \text{ km}] \times [-3000 \text{ km}, 3000 \text{ km}]$. Unless stated otherwise, $z = 0$ corresponds to the surface. In Equations 4–9, however, we use the convention $z = 0$ at the reference tropopause height (z_{trop}).

Text S2: Sea surface temperature fields

In all experiments, the atmospheric model is forced by a sea surface temperature (SST) field of the following form:

$$\text{SST}(x, y) = \text{SST}_{\text{eq}} - \frac{\Delta\text{SST}}{2}\left[1 + \tanh\left(2\frac{g_{\text{SST}}}{\Delta\text{SST}}(y - y^*(x))\right)\right] \tag{1}$$

where $\text{SST}_{\text{eq}} = 21°\text{C}$ is the temperature at the southern boundary, and $\Delta\text{SST} = 15°\text{C}$ is the SST difference between the northern and the southern boundaries. $g_{\text{SST}} = 3°\text{C (100 km)}^{-1}$ is the maximum SST gradient in absolute value. The SST function of $y - y^*(x)$ is shown in Figure S1a. The function $y^*(x)$ defines the shape of the SST front, which varies across experiments:

$$y^*_{\text{CTL}}(x) = 0 \quad \forall\, x \tag{2}$$

$$y^*_{\text{M}}(x) = \begin{cases} \frac{l_{\text{SST}}}{2} \sin\left(\pi \frac{x - x_{\text{SST}}}{l_{\text{SST}}}\right) & \text{for } x \in [x_{\text{SST}}, x_{\text{SST}} + \Delta x_{\text{SST}}] \\ 0 & \text{else} \end{cases} \tag{3}$$

where $y^*_{\text{CTL}}(x)$ is a zonal SST front, and $y^*_{\text{M}}(x)$ represents a meandering SST front (Figure S1b). The typical meander size, l_{SST}, is 500 km in M5 and 1000 km in M10 (Fig-

ure S1b). In both M5 and M10, the meanders begin at $x_{\mathrm{SST}} = 1000$ km, and extend zonally over 4000 km.

Text S3: Initial atmospheric state

The initial atmospheric state is adapted from Bui and Spengler (2021) and consists of a zonally symmetric jet and a cyclonic perturbation, as presented in Figure S2. As detailed below, the thermal wind balance is imposed to fully determine the initial state from reference temperature, pressure, and wind profiles (Plougonven & Zeitlin, 2009). The jet is defined by a wind field $\overline{u}(y, z)$ (Equations 4-9), a vertical potential temperature profile $\overline{\theta}(y_{\mathrm{ref}}, z)$ (Equation 10), and a reference pressure $\overline{p}(y_{\mathrm{ref}}, 0) = p_0$ (Table S1). The reference latitude is set to $y_{\mathrm{ref}} = -3000$ km, corresponding to the southern boundary. All constants and their descriptions are provided in Table S1. As mentioned above, the jet is defined by the following set of equations:

$$\overline{u}(y, z) = U_0 \, W_y(y) \, W_z(z^*) \tag{4}$$

$$W_y(y) = \begin{cases} \cos^2\left(\frac{\pi}{2} \frac{y - y_{\mathrm{jet}}}{L_y}\right) & \text{for } |y - y_{\mathrm{jet}}| \leq L_y \\ 0 & \text{else} \end{cases} \tag{5}$$

$$z^*(y, z) = z - A \tanh\left(\frac{5}{2} \frac{y_{\mathrm{jet}} - y}{L_y}\right) \tag{6}$$

$$A(z) = \begin{cases} 0 & \text{for } z < -L_z \\ |z_{\mathrm{jet}} - z_{\mathrm{trop}}| \sin\left(\frac{\pi}{2} \frac{L_z + z}{L_z}\right) & \text{for } -L_z \leq z \leq 0 \\ |z_{\mathrm{jet}} - z_{\mathrm{trop}}| & \text{for } z > 0 \end{cases} \tag{7}$$

$$W_z(z) = \begin{cases} 1 + C(\frac{z}{l_1})^2[\frac{1}{6}(\frac{z}{l_1})^2 - 1] & \text{for } |z| \le l_1 \\ w_0 - \alpha|z| & \text{for } l_1 < |z| < L_z - l_2 \\ \frac{\alpha l_2}{2}(\frac{L_z - |z|}{l_2})^3(2 - \frac{L_z - |z|}{l_2}) & \text{for } L_2 - l_2 \le |z| \le L_z \\ 0 & \text{for } |z| > L_z \end{cases} \tag{8}$$

with

$$l_1 = l_2 = 0.04\, L_z,\ w_0 = \frac{1}{1 - \frac{3}{8}\frac{l_1}{L_z - 0.5\, l_2}},\ C = \frac{3}{4}\alpha l_1 \text{ and } \alpha = \frac{w_0}{L_z - 0.5\, l_2} \tag{9}$$

$\overline{\theta}$ is defined as follows:

$$\overline{\theta}(y = y_{\text{ref}}, z) = \begin{cases} \theta_0 \exp\left(\frac{N^2_{\text{trop}}\, z}{g}\right) & \text{for } z \le z_{\text{trop}} \\ \theta(y_{\text{ref}}, z_{\text{trop}}) \exp\left(\frac{N^2_{\text{stra}}(z - z_{\text{trop}})}{g}\right) & \text{for } z > z_{\text{trop}} \end{cases} \tag{10}$$

The cyclonic perturbation is defined as an axisymmetric pressure anomaly centered at (x_p, y_p):

$$p'(x, y, z) = \begin{cases} \Delta p \cos^2(\frac{\pi}{2}\frac{z}{H_p})(1 - R^2)^3 & \text{for } R < 1 \text{ and } z < H_p \\ 0 & \text{else} \end{cases} \tag{11}$$

where $R = \sqrt{(x - x_p)^2 + (y - y_p)^2}/R_p$. Applying the hydrostatic balance yields the density anomaly:

$$\rho'(x, y, z) = \begin{cases} \frac{\pi \Delta p}{2 g H_p} \sin(\pi \frac{z}{H_p})(1 - R^2)^3 & \text{for } R < 1 \text{ and } z < H_p \\ 0 & \text{else} \end{cases} \tag{12}$$

The moisture content is initialized using a vertical profile of relative humidity:

$$\mathrm{rh}(z) = \mathrm{rh}_0 \exp\Big[-0.5\Big(\frac{z}{z_{\mathrm{rh}}}\Big)^4\Big] \tag{13}$$

The full initial state—that is, the zonal jet plus the perturbation—is determined using geostrophic and hydrostatic balances coupled with the ideal gas law. We proceed as follows:

• First, we perform a numerical integration using a 4th-order Runge-Kutta scheme (RK4) to impose hydrostatic balance, coupled with the ideal gas law. Starting from a reference potential temperature profile $\overline{\theta}(y_{\mathrm{ref}}, z)$ and a surface pressure $\overline{p}(y_{\mathrm{ref}}, 0) = p_0$, we compute the reference pressure profile $\overline{p}(y_{\mathrm{ref}}, z)$ for all z. The corresponding reference density $\overline{\rho}(y_{\mathrm{ref}}, z)$ is then obtained via the equation of state.

• Second, we apply successive RK4 integrations of the geostrophic and hydrostatic balances to determine the full jet fields: $\overline{p}(y, z)$, $\overline{\theta}(y, z)$, and $\overline{\rho}(y, z)$. At iteration i, the pressure field $\overline{p}_i(y, z)$ is computed from $\overline{\theta}_{i-1}(y, z)$ and the zonal wind $\overline{u}$ via the geostrophic balance. For the first iteration, we initialize $\overline{\theta}_0(y, z) = \overline{\theta}(y_{\mathrm{ref}}, z)$ for all y. The density field $\overline{\rho}_i(y, z)$ is then computed from $\overline{p}_i(y, z)$ via the hydrostatic balance, and the updated potential temperature field $\overline{\theta}_i(y, z)$ is derived using the ideal gas law. We perform 10 iterations to ensure convergence.

• Finally, we construct the full fields by adding perturbations: $p = \overline{p} + p'$ and $\rho = \overline{\rho} + \rho'$. The temperature is obtained from the ideal gas law, and the full wind field (u, v) is diagnosed using geostrophic balance. The water vapor mixing ratio is calculated from the

relative humidity profile and taken into account in the equation of state via the virtual temperature.

References

Bui, H., & Spengler, T. (2021). On the influence of sea surface temperature distributions on the development of extratropical cyclones. *Journal of the Atmospheric Sciences*, *78*(4), 1173–1188.

Klemp, J., Dudhia, J., & Hassiotis, A. (2008). An upper gravity-wave absorbing layer for nwp applications. *Monthly Weather Review*, *136*(10), 3987–4004.

Plougonven, R., & Zeitlin, V. (2009). Nonlinear development of inertial instability in a barotropic shear. *Physics of fluids*, *21*(10).

Table S1. Physical parameters of the initial atmospheric state

Name	Value	Description
f	$1,028 \times 10^{-4}$ s^{-1}	Coriolis parameter of the f-plane at 45°N
U_0	50 m.s^{-1}	Jet maximum wind speed
z_{jet}	8 km	Altitude of the jet core
L_y	1000 km	Meridional extent of the jet
L_z	10 km	Vertical extent of the jet
p_0	1008 hPa	Sea level pressure at the southern boundary
θ_0	295 K	Surface potential temperature at the southern boundary
z_{trop}	10 km	Tropopause height at the southern boundary
N^2_{trop}	10^{-4} s^{-2}	Static stability in the troposphere
N^2_{stra}	5.6×10^{-4} s^{-2}	Static stability in the stratosphere
rh_0	0.5	Relative humidity at the surface
z_{rh}	8 km	Vertical extent of the relative humidity profile
R_p	500 km	Radius of the initial perturbation
H_p	6 km	Vertical extent of the initial perturbation
Δp	2 hPa	Magnitude of the initial perturbation
x_p	0 km	Initial location of the perturbation along the x-axis
y_p	0 km	Initial location of the perturbation along the y-axis

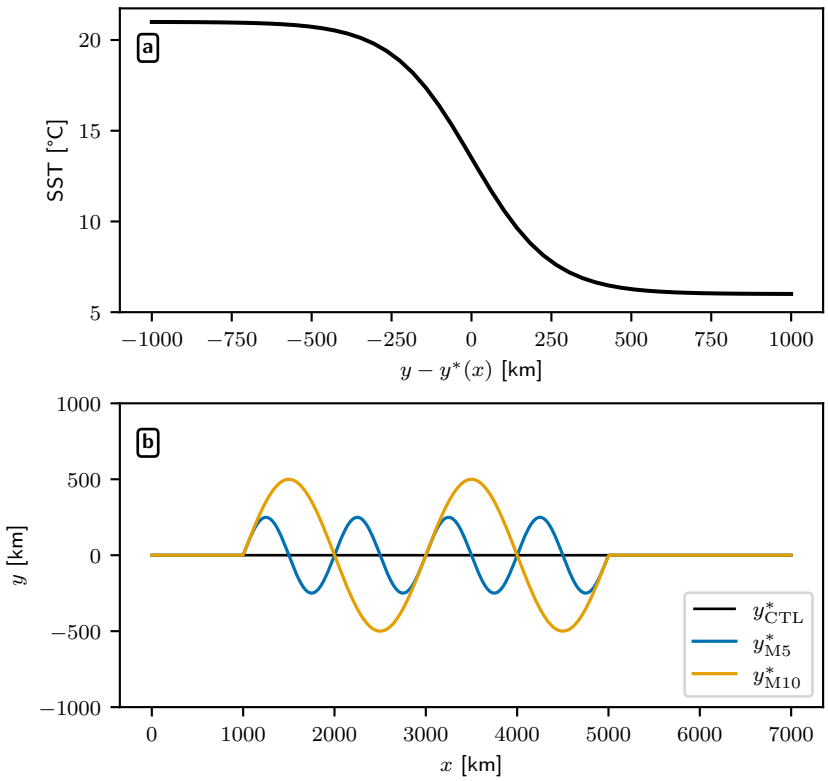

Figure S1. Idealized sea surface temperature fronts. (a) SST profile as a function of $y - y^*(x)$ (Equation 1). (b) Shape of the SST fronts ($y^*(x)$, Equations 2 and 3) for CTL (black), M5 (blue) and M10 (orange).

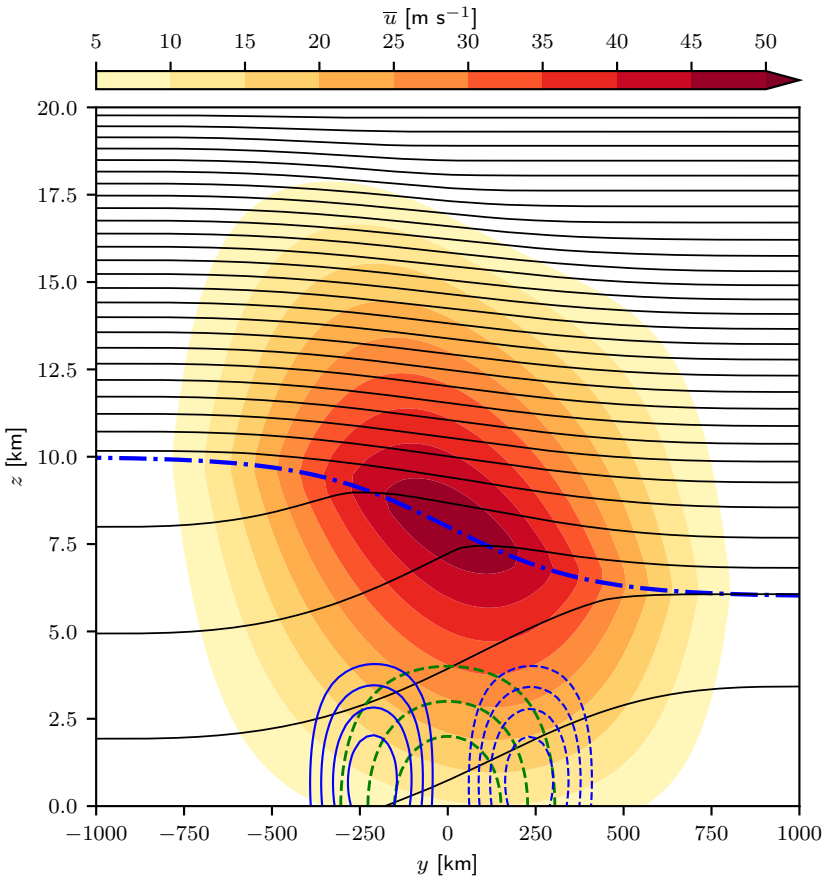

Figure S2. Idealized initial atmospheric state. Jet stream zonal wind ($\overline{u}$, shading) and potential temperature ($\overline{\theta}$, black contours from 300 K to 570 K every 10 K). Tropopause height (dash-dotted blue line), pressure perturbation ($p'(x_p, y)$, green contours at -1.5, -1, and -0.5 hPa) and associated zonal wind perturbation ($u - \overline{u}$, blue contours from -5 to -2 m s^{-1} and from 2 to 5 m s^{-1}). Dashed contours indicate negative values.

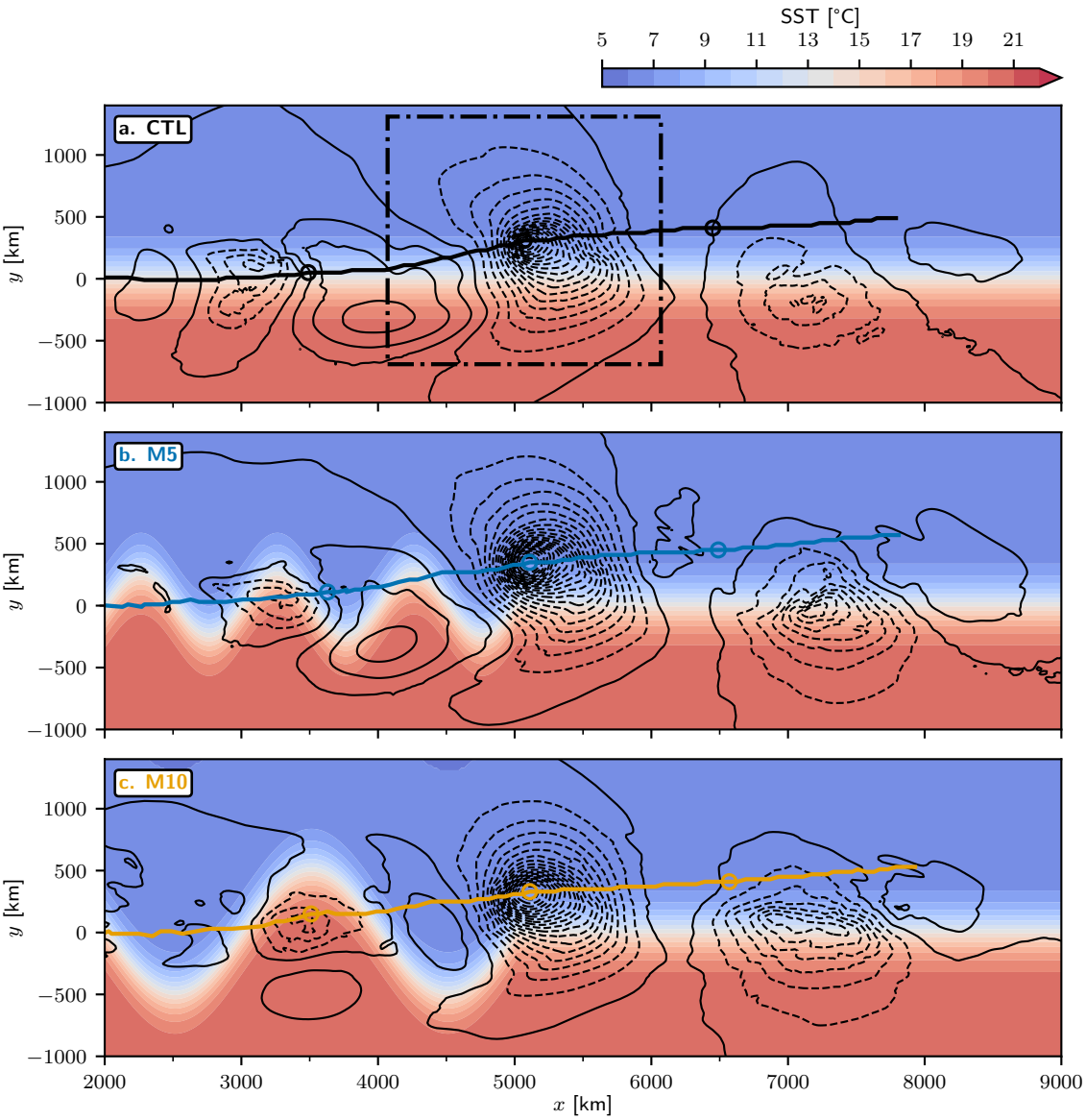

Figure S3. Upstream and downstream cyclone development. (a) CTL, (b) M5, and (c) M10 experiments. The primary cyclone trajectory (solid line) is marked at 48, 72, and 96 h with circles. SST (color shading) and sea level pressure (SLP) anomaly at 72 h (black contours from -22 hPa to 3 hPa every 1 hPa, dashed for negative values). The SLP anomaly field highlights upstream and downstream cyclones located approximately 2000 km west and east of the primary cyclone, respectively. In (a), the dash-dotted square represents the cyclone domain at 72 h for CTL.

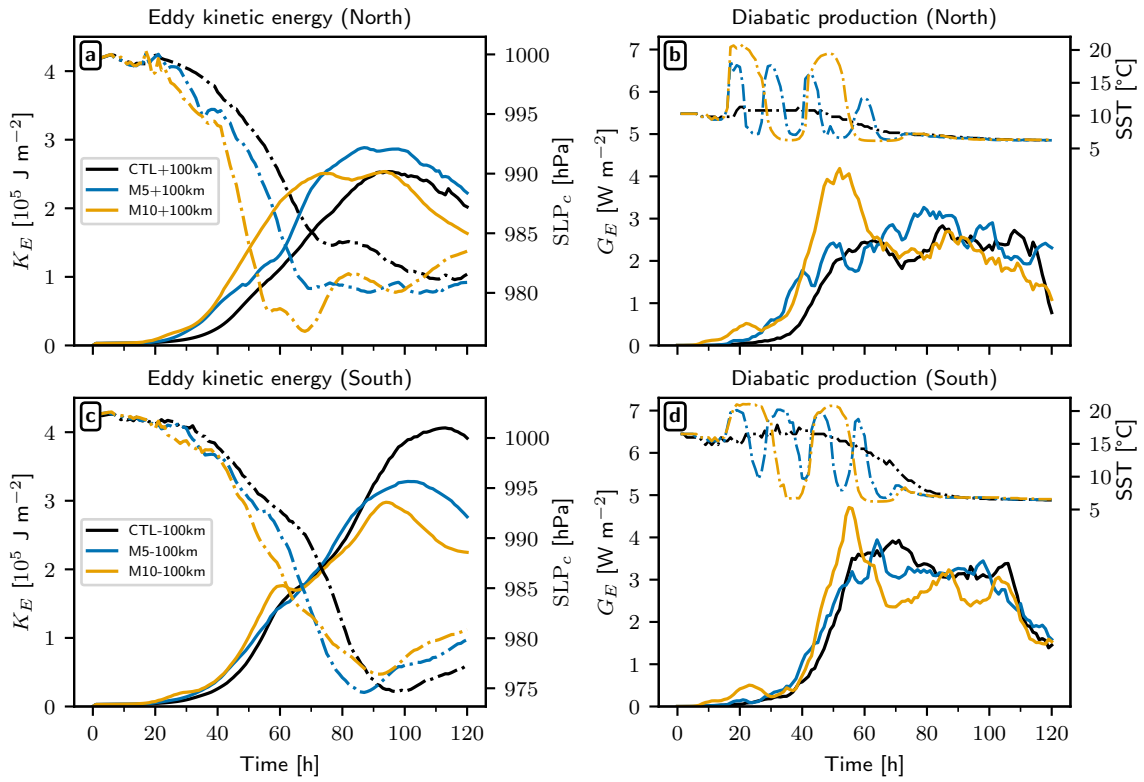

Figure S4. Sensitivity to a northward and southward shift of 100 km. Experiments with the initial cyclonic perturbation shifted 100 km northward (a, b) and southward (c, d). (a, c) Eddy kinetic energy (K_E, solid lines) and sea level pressure at the cyclone center (SLP$_c$, dash-dotted lines). (b, d) Diabatic production (G_E, solid lines) of eddy available potential energy and SST underneath the cyclone center (dash-dotted lines). K_E and G_E are vertically integrated and horizontally averaged quantities over the cyclone domain (see Methods). Black, blue and orange lines correspond to CTL, M5±100km and M10±100km experiments, respectively. The cyclone response to ocean meanders in the set +100 km (respectively -100 km) is stronger (resp. weaker) than in the main text, as the cyclone encounters greater (resp. lower) SST anomalies (b).

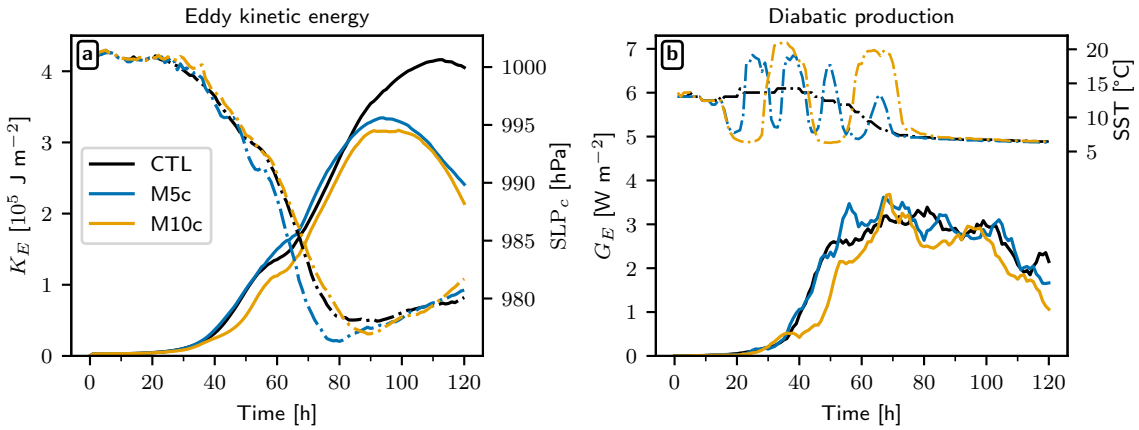

Figure S5. Sensitivity to an opposite SST configuration. (a) Eddy kinetic energy (K_E, solid lines) and sea level pressure at the cyclone center (SLP$_c$, dash-dotted lines). (b) Diabatic production (G_E, solid lines) of eddy available potential energy and SST underneath the cyclone center (dash-dotted lines). K_E and G_E are vertically integrated and horizontally averaged quantities over the cyclone domain (see Methods). Black, blue and orange lines correspond to CTL, M5c and M10c experiments, respectively. In M5c and M10c, cold and warm SST anomalies associated with the meanders are reversed compared to M5 and M10 in the main text.